Dual-output modulation in time-wavelength interleaved photonic analog-to-digital converter based on actively mode-locked laser

Huajie Zhang (张华杰)[1], Weiwen Zou (邹卫文)[1,2,*], Guang Yang (杨 光)[1], and Jianping Chen (陈建平)[1,2]

[1]*State Key Laboratory of Advanced Optical Communication Systems and Networks, Department of Electronic Engineering, Shanghai Jiao Tong University, Shanghai 200240, China*

[2]*Shanghai Key Lab of Navigation and Location Services, Shanghai Jiao Tong University, Shanghai 200240, China*

**Corresponding author: wzou@sjtu.edu.cn*

Received October 26, 2015; accepted January 8, 2016; posted online February 26, 2016

This Letter demonstrates the application of dual-output modulation in a photonic analog-to-digital converter (PADC) with a high sampling rate and resolution. The PADC is time-wavelength interleaved and based on an actively mode-locked laser. According to theoretical analysis, the dual-output PADC system shows a better linearity for achieving a higher dynamic range. In the experiment, third-order distortion is significantly suppressed by ~40 dB when the dual-output modulator is used and the effective number of bits of the PADC has reached 9.0 bits below 0.2 GHz and 6.4 bits at 6.1 GHz in our PADC with a sampling rate of 20 GS/s.

OCIS codes: 060.5625, 230.0250, 250.4745, 140.4050.

doi: 10.3788/COL201614.030602.

Analog-to-digital converters (ADCs) have been playing an important role in radar, communication systems, and many other fields. The demand of an ADC with a high sampling rate and high resolution is rather intense. While great progress has been made in the field of electronic ADC (EADC), the performance of EADC is still limited by the timing jitter of electronic clocks[1,2]. Photonic ADC (PADC) has advantages of higher stability and lower timing jitter, which can essentially improve the performance of ADC and overcome the bottleneck of EADC[3–6]. In order to achieve a compact and practical PADC, electronic-optical integration technology has been partially demonstrated although the sampling rate in the integrated photonic PADC is still low due to the limited channels[7,8]. A PADC can be realized by either an actively mode-locked laser (AMLL)[9] or a passively mode-locked laser (PMLL)[10–12]. In comparison, the repetition of the AMLL reaches several GHz and can be easily changed by the external radio frequency (RF) signal. Moreover, the timing jitter of the AMLL can also reach the order of ~fs[13]. Time-division demultiplexing[14] and time-wavelength interleaving[15,16] schemes are effective ways to achieve a high-sampling-rate PADC based on an AMLL. A PADC based on an AMLL with a time-wavelength interleaving scheme[15,16] achieves a higher sampling rate and shows better stability. The input RF signal is usually sampled via an electro-optic intensity modulator (EOM), but its inherent sinusoidal transfer function induces nonlinearity in the PADC. When operating at a large modulation index, a higher odd-order distortion appears and degrades the dynamic range[17]. Dual-output modulation and arcsine operation has been used to suppress the third-order distortion in a PADC based on PMLL[18] or in a single-channel PADC based on an AMLL[19]. However, the effectiveness has not been demonstrated in a time-wavelength interleaved PADC based on an AMLL.

In this Letter, the dual-output modulation method in a time-wavelength interleaved PADC based on an AMLL with a high resolution is analyzed theoretically and verified experimentally. A high sampling rate of 20 GS/s is achieved by adopting a 2-parallel-channel time-wavelength interleaved PADC based on a 10 GHz AMLL.

The architecture of a time-wavelength interleaved PADC based on dual-output modulation is shown in Fig. 1(a). The optical pulse from an AMLL (Calmar PSL-10-TT) has a repetition rate of 10 GHz, and its spectrum is broadened by a pulse compressor (Calmar PCS-2). As shown in Fig. 1(b), the sampling rate of the optical pulse train is N times multiplied via the time-wavelength interleaving method. The broadened spectrum is sliced into N channels by a $1 \times N$ wavelength-division multiplexer (WDM). Precise adjustment of the tunable delay line (TDL) and the variable optical attenuator (VOA) in each channel is able to achieve a time-wavelength interleaved optical sampling clock with a sampling rate multiplied by N times when all channels are reflected back by a Faraday rotator mirror (FRM) and combined via the WDM[16]. The sampling clock is amplified by an erbium-doped fiber amplifier (Calmar AMP-ST18). A dual-output Mach–Zehnder EOM (EOSPACE AZ-1X2-AV5-40-PFA-SFA) is employed to implement the sampling process. The quantization and data acquisition process is described in Fig. 1(c). The differential sampled signal is separated into 2N parallel channels via two WDMs. The optical signal in all channels turns into an electronic signal via a photodetector (PD) array and then is digitized by an EADC

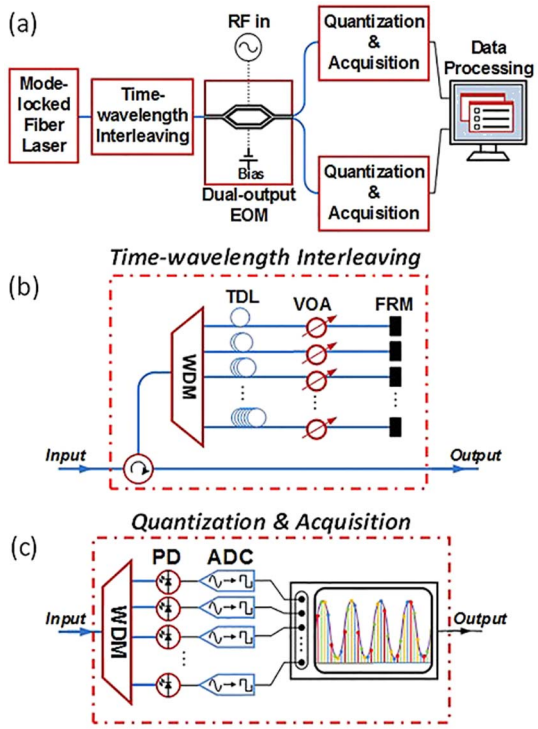

Fig. 1. (a) Experimental configuration of the PADC, (b) schematic of time-wavelength interleaving, and (c) schematic of parallel quantization and data acquisition.

(Keysight DSOS804A). Finally, the RF signal is recovered by digital calibration and processing.

The ideal sampling clock of a PADC is described as

$$p(t) = P_0 \sum_{m=-\infty}^{+\infty} \delta(t - mT_s), \tag{1}$$

where P_0 is the amplitude of the optical sampling clock and $T_s = 1/f_s$ is the period of the optical clock.

For a dual-output modulator, the transfer function for one arm $T_{M,1}$ and the other $T_{M,2}$ can be expressed by

$$T_{M,1}(V_M) = \frac{1}{2} + \frac{1}{2}\cos\left[\frac{\pi}{V_\pi}(V_M + V_{B,1})\right],$$
$$V_{B,1} = -\frac{V_\pi}{2}, \tag{2}$$

$$T_{M,2}(V_M) = \frac{1}{2} + \frac{1}{2}\cos\left[\frac{\pi}{V_\pi}(V_M + V_{B,2})\right],$$
$$V_{B,2} = \frac{V_\pi}{2}, \tag{3}$$

where V_π is the half-wave voltage of the modulator and $V_M(t) = V_0 \cos \Omega_M t$ denotes the input RF signal with frequency f_M and amplitude V_0. It is worth noting that the transmittance for a single-output modulator is expressed by Eq. (2).

The equivalent transmittance of the dual-output modulator is described as

$$T_M(V_M) = \arcsin\left(\frac{T_{M,1} - T_{M,2}}{T_{M,1} + T_{M,2}}\right) = \arcsin\left(\sin\left(\frac{\pi V_M}{V_\pi}\right)\right). \tag{4}$$

From Eq. (2), we can get the signal modulated by a single-output modulator as

$$p_m(t) = \frac{1}{2} + \sum_{m=0}^{\infty}(-1)^m J_{2m+1}(M)\cos[(2m-1)\Omega_M t], \tag{5}$$

where $M = \pi V_0/V_\pi$ denotes the modulation index and $J_n(\cdot)$ is the nth-order Bessel function. It is shown in Eq. (5) that the nonlinearity of a single-output modulator induces higher odd-order harmonics of the input frequency.

Assume that the bandwidth of the PD is large enough. In this case, after detection, the sampled optical signal is demonstrated by

$$p_s(t) = GR_{\mathrm{PD}}p_m(t), \tag{6}$$

where G is the gain (or loss) of the converted electrical signal and R_{PD} is the responsivity of the PD.

Finally, the process of quantization can be described in mathematics as follows:

$$p_Q[k] = p_s(kT_s). \tag{7}$$

Equation (7) can be expanded as

$$p_Q[k] = GR_{\mathrm{PD}}P_0\left[\frac{1}{2} + \sum_{m=0}^{\infty}(-1)^m J_{2m+1}\left(\frac{\pi V_0}{V_\pi}\right) \times \cos[(2m-1)k\Omega_M T_s]\right]. \tag{8}$$

As demonstrated in Eq. (8), the distortion induced by a modulator results in the high-order harmonics into the input RF signal. Hence, the nonlinearity of the modulator can be characterized by the distortion-signal power ratio (δ_{PADC}), which is defined by

$$\delta_{\mathrm{PADC}} = \frac{P_{\mathrm{high-order\,hamonics}}}{P_{\mathrm{signal}}}, \tag{9}$$

where $P_{\mathrm{high-order\,hamonics}}$ is the power of the higher-order harmonics and P_{signal} is the signal power.

According to the theoretical model, the signal-to-noise-and-distortion (SINAD) for the single-output modulator is demonstrated by

$$\mathrm{SINAD} = 10\log\frac{\frac{\sigma_a^2}{2\mu} + (1+\gamma^2)}{\frac{\sigma_a^2}{2\mu} + 4\pi^2(f_M/f_S)^2\sigma_t^2 + \gamma^2}, \tag{10}$$

where $\mu = J_1(M)$ and $\gamma = J_3(M)/J_1(M)$, σ_a (σ_t) is representative of the root mean square of the amplitude (clock

timing) mismatch, and f_s is the sampling rate of the PADC. For the SINAD with a dual-output modulation, the nonlinearity is cancelled and the parameters in Eq. (10) become $\mu = M/2$ and $\gamma = 0$.

According to the IEEE standard for the terminology and test methods for ADCs[20], the effective number of bits (ENOB) can be derived from

$$\mathrm{ENOB} = \frac{\mathrm{SINAD} - 1.76}{6.02}. \tag{11}$$

The simulated transmittance of the dual-output and single-output modulation based on Eqs. (2) and (9) is depicted in Fig. 2(a). The distortion-signal power ratio (δ_{PADC}) calculated by Fourier transform is plotted in Fig. 2(b) as a function of the modulation index (M). From Fig. 2(a) and 2(b), one can see that the linear region of the transmittance (i.e., the dynamic range) of the dual-output modulator is significantly increased.

In order to estimate the spurious free dynamic range (SFDR) of the modulator, we sample a 3.1 GHz single-tone RF signal and set $M = 0.5$ to artificially worsen the third-order distortion. In the experiment, a 1×2 WDM is employed as an example to obtain a PADC with a 20 GS/s sampling rate. The experimental time domain signal and the spectra for single-output and dual-output modulations are described in Figs. 3 and 4, respectively. Although the difference in time domain (see Fig. 3) is indistinct, the contrast in frequency domain (see Fig. 4) is clear. As depicted in Fig. 4(a), the spectrum is composed of a 3.1 GHz signal, interleaving distortion, and third-order distortion. In comparison, Fig. 4(b) illustrates that the third-order distortion is significantly suppressed by ~40 dB when the dual-output modulator is used.

It is worth noting that interleaving distortion has been reduced to a relatively low level by employing the channel-mismatching analysis model[21] and tuning of the TDL and VOA in the PADC system. Interleaving distortion arises at $f = kf_s/N \pm (2m-1)f_m (k = 1, 2, \ldots N-1, m = 1, 2, 3\ldots)$ due to the amplitude and timing mismatches in each channel, where N is the number of time-wavelength

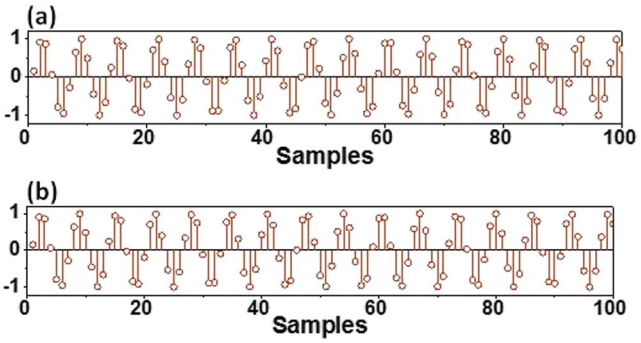

Fig. 3. Experimental time-domain signal for (a) single-output modulation and (b) dual-output modulation.

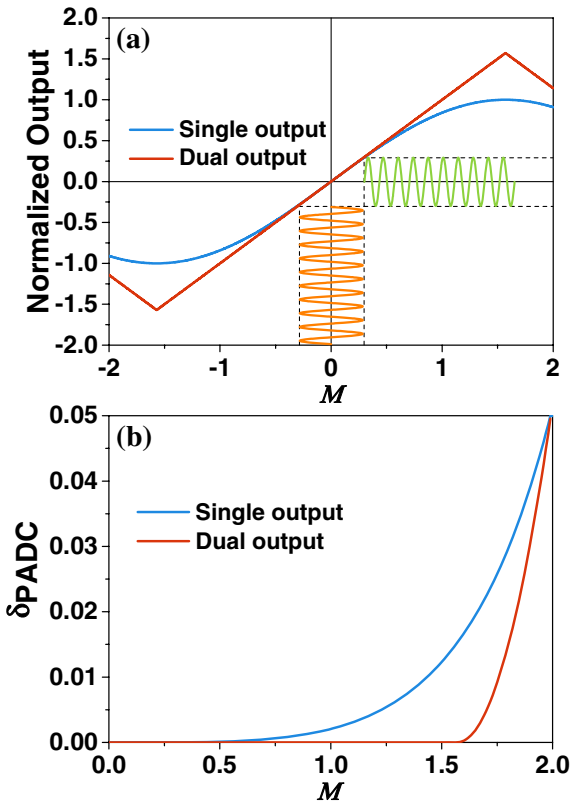

Fig. 2. Simulation results. (a) Transmittance of dual-output and single-output modulation and (b) noise-signal power ratio versus modulation index.

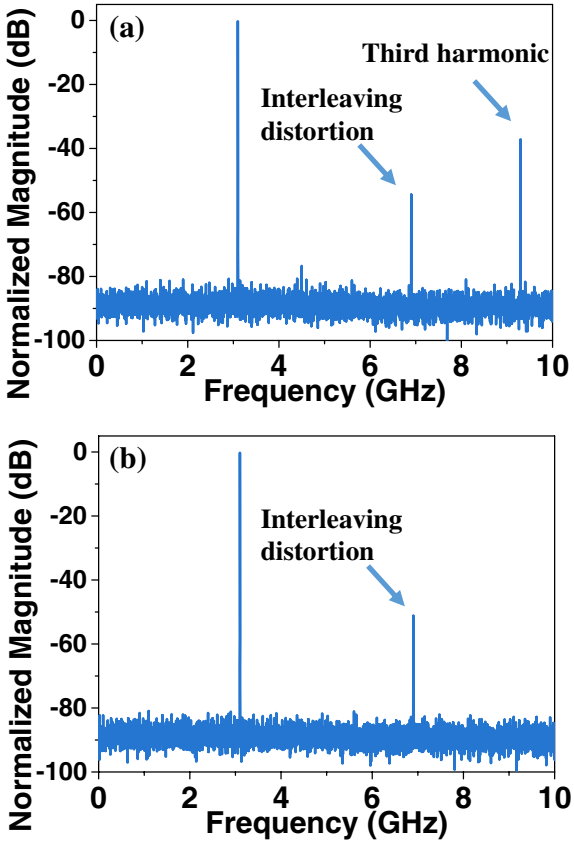

Fig. 4. Experimental spectrum for (a) single-output modulation and (b) dual-output modulation.

interleaved channels and f_m is the input RF frequency. The amplitude and timing mismatches of $a_n = |p_0 + p_1 e^{j\pi(n-1)}|$ and $\Delta t_n = \frac{1}{\Omega_M}\arg[p_0 + p_1 e^{j\pi(n-1)}](n = 1, 2)$, where p_0 is the recovered RF signal and p_1 represents the component at $f = f_s/2 - f_m$, are deduced from the power spectra in Fig. 4. Later, the amplitude and timing mismatches are properly tuned by the VOA and TDL in each channel, respectively.

The achieved ENOB for the PADC based on single-output and dual-output modulations are illustrated in Fig. 5, respectively. The contours are calculated according to the theoretical model as described by Eqs. (10) and (11). The marked values represent the experimental results, which agree well with the theoretical results. When operating at a small M, there is almost no difference between single-output and dual-output modulations, while for large M dual-output modulation shows a significant advantage over single-output modulation because of its better linearity and larger SFDR (see Fig. 2). The highest ENOB in Fig. 5(a) is limited to 7 bits due to the harmonic order distortions caused by single-output modulator. As depicted in Fig. 5(b), dual-output modulation breaks this limitation and reaches 9 bits. For instance, for the input RF frequency of 0.2 GHz, the ENOB is 9 bits for dual-output modulation while only 6.3 bits for single-output modulation. Even for high RF frequency of 6.1 GHz, the ENOB is 6.4 bits for dual-output modulation while only 5.8 bits for single-output modulation.

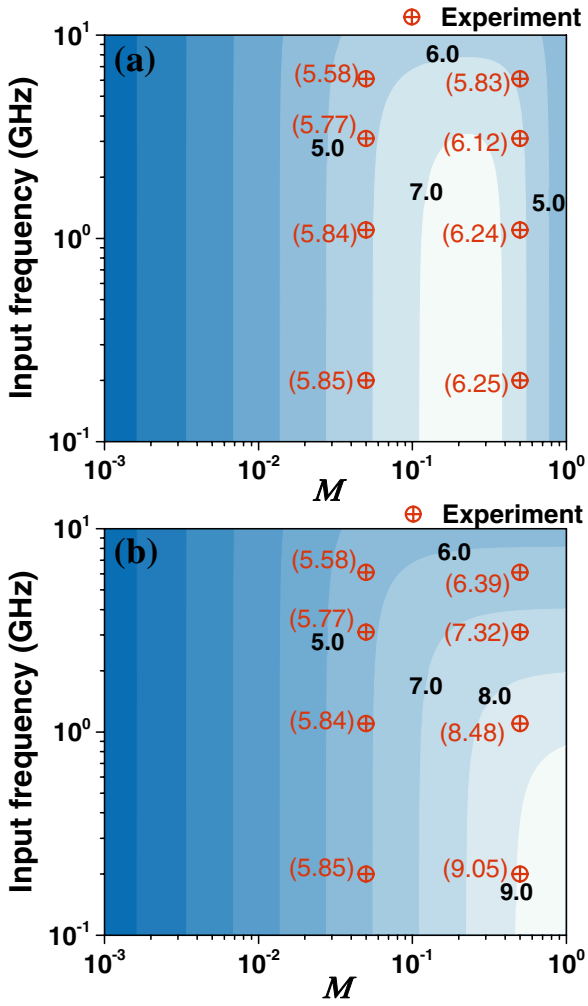

Fig. 5. Simulation and experiment of the ENOB for (a) single-output modulation and (b) dual-output modulation.

In conclusion, we demonstrate that dual-output modulation can effectively suppress higher odd-order distortions and improve the performance of the time-wavelength interleaved PADC based on AMLL. In the experiment, a 1 × 2 WDM is employed here as an example to accomplish a 20 GS/s PADC based on a 10 GHz AMLL. The third-order distortion is suppressed by ~40 dB. The ENOB in the PADC reached 9.0 bits below 0.2 GHz and 6.4 bits at 6.1 GHz. Furthermore, the dual-output modulation method for a PADC with more interleaved channels and a higher repetition rate is now under investigation.

This work was supported by the National Natural Science Foundation of China (Nos. 61535006 and 61571292), the Specialized Research Fund within the Doctoral Program through the Ministry of Education (No. 20130073130005), and the State Key Laboratory Project of Shanghai Jiao Tong University (No. 2014ZZ03016).

References

1. G. C. Valley, Opt. Express **15**, 1955 (2007).
2. R. H. Walden, in *Wiley Encyclopedia of Computer Science and Engineering* **126** (2008), http://onlinelibrary.wiley.com/doi/10.1002/9780470050118.ecse014/full.
3. A. O. Wiberg, in *Proceedings Optical Fiber Communication Conference* (2015), paper M2E.1.
4. Y. Wang, Y. Dou, and H. Zhang, Chin. Opt. Lett. **11**, 042301 (2013).
5. Y. Wang, H. Zhang, Y. Dou, and M. Yao, Chin. Opt. Lett. **11**, 082301 (2013).
6. B. Xu, W. Lv, J. Ye, J. Zhou, X. Jin, X. Zhang, H. Chi, and S. Zheng, Photon. Res. **2**, 97 (2014).
7. A. Khilo, S. J. Spector, M. E. Grein, A. H. Nejadmalayeri, C. W. Holzwarth, M. Y. Sander, M. S. Dahlem, M. Y. Peng, M. W. Geis, N. A. DiLello, J. U. Yoon, A. Motamedi, J. S. Orcutt, J. P. Wang, M. C. Sorace Agaskar, M. A. Popović, J. Sun, G. Zhou, H. Byun, J. Chen, J. L. Hoyt, H. I. Smith, R. J. Ram, M. Perrott, T. M. Lyszczarz, E. P. Ippen, and F. X. Kärtner, Opt. Express **20**, 4454 (2012).
8. F. Kärtner, A. Khilo, and A. Nejadmalayeri, in *Optical Fiber Communication Conference and Exposition and the National Fiber Optic Engineers Conference* (2013), pp. 17.
9. W. Ng, R. Stephens, D. Persechini, and K. V. Reddy, Electron. Lett. **37**, 113 (2001).
10. T. R. Clark, J. U. Kang, and R. D. Esman, IEEE Photon. Technol. Lett. **11**, 1168 (1999).
11. X. Zou, Y. Leng, Y. Li, Y. Feng, P. Zhang, Y. Hang, and J. Wang, Chin. Opt. Lett. **13**, 081405 (2015).
12. X. Li, W. Zou, G. Yang, and J. Chen, IEEE Photon. Technol. Lett. **27**, 93 (2015).
13. F. Quinlan, S. Gee, S. Ozharar, and P. J. Delfyett, Opt. Lett. **31**, 2870 (2006).
14. T. R. Clark and M. L. Dennis, IEEE Photon. Technol. Lett. **13**, 236 (2001).

15. W. Ng, L. Luh, D. L. Persechini, D. Le, Y. M. So, M. Mokhtari, C. H. Fields, D. Yap, and J. E. Jensen, Proc. SPIE **5435**, 171 (2004).
16. G. Yang, W. Zou, X. Li, and J. Chen, Opt. Express **23**, 2174 (2015).
17. J. C. Twichell and R. Helkey, IEEE Photon. Technol. Lett. **12**, 1237 (2000).
18. P. W. Juodawlkis, J. C. Twichell, G. Betts, J. J. Hargreaves, R. D. Younger, J. L. Wasserman, F. J. O'Donnell, K. G. Ray, and R. C. Williamson, IEEE Trans. Microwave Theory Tech. **49**, 1840 (2001).
19. J. H. Wong, S. Aditya, H. Q. Lam, P. H. Lim, K. E. K. Lee, and P. S. Ping, in *2012 IEEE International Topical Meeting on Microwave Photonics (MWP)* (2012), pp. 204.
20. IEEE collaboration, "IEEE Standard for Terminology and Test Methods for Analog-To-Digital Converters," IEEE Std 1241-2000, http://ieeexplore.ieee.org/xpl/articleDetails.jsp?arnumber=929859&contentType=Standards (2000).
21. G. Yang, W. Zou, H. Zhang, and J. Chen, "Theoretical and experimental analysis of a high speed time-wavelength interleaved photonic analog-to-digital converter," J. Lightwave Technol. (submitted).